ASTM A-335 P9 is widely employed within the piping infrastructure of the crude distillation unit for the conveyance of heavy vacuum gas oil (HVGO) crude residue before subsequent downstream processing, owing to its high mechanical properties.

Due to elevated operating temperatures, the presence of sulfur, the material remains vulnerable to naphthenic acid corrosion, which can compromise its structural and operational integrity. This study examines the material's response to the application of eco-enzyme as a green corrosion inhibitor (GCI) employing extensive several tests under naphthenic acid distillate which collected and processed from the heavy vacuum gas oil piping. optical emission spectroscopy (OES), ultraviolet-visible spectroscopy (UV-Vis), and Fourier rransform infra-red (FTIR) equipped with potentiodynamic polarization and electrochemical impedance spectroscopy (EIS) to dive into the corrosion resistance of EE inhibitor under the naphthenic acid extracts. Moreover, the scanning electronic microscopy and energy X-Ray dispersive (SEM-EDX) was utilized to reveal the surface morphology and the elemental identity of the retained inhibition mechanism. Based on the OES, the presence of Cr and Mo are highlighted with the composition of 9.135% and 0.894% which aligned with the 9Cr-1Mo material specification. The electronic transition of π-π* and n-π* transitions is in good agreement with the presence of aromatic -OH, C-H sp3, R-CHO, C=O, C-O and aromatic absorption at 525 nm, which correlates with peaks observed in FTIR spectra at 3200–3400, 2800–3000 cm^{-1}. The high inhibition efficiency beyond 77% is correlated to the adsorption of the inhibitor that thermodynamically adheres to the Langmuir adsorption isotherm and applicable of model the HVGO system

Keywords: green corrosion inhibitor, biomass, eco-enzyme, Langmuir isotherm, adsorption, refinery

UDC 620.193:66.094.3:665.6
DOI: 10.15587/1729-4061.2025.347916

DEVELOPMENT OF A PRELIMINARY MODEL FOR ADDRESSING NAPHTHENIC ACID CORROSION OF ASTM A-335 P9 USING AN ECO-ENZYME GREEN INHIBITOR ON HEAVY-VACUUM GAS OIL RESIDUE

Kadek Ambara Jaya
Postgraduate Student*
Johny Soedarsono
Corresponding author
Doctor of Engineering, Professor
Prof. Johny Wahyuadi Laboratory*
E-mail: jwsono@metal.ui.ac.id
Yudha Pratesa
Doctor of Engineering
Prof. Johny Wahyuadi Laboratory*
Rini Riastuti
Doctor of Engineering, Senior Lecturer
Prof. Johny Wahyuadi Laboratory*
Agus Kaban
Doctor of Engineering
Prof. Johny Wahyuadi Laboratory*
*Department of Materials and Metallurgical Engineering
Universitas Indonesia
Kampus Baru UI Depok, Jawa Barat, Indonesia, 16424

Received 09.10.2025
Received in revised form 20.11.2025
Accepted date 16.12.2025
Published date 30.12.2025

How to Cite: *Jaya, K. A., Soedarsono, J. W., Pratesa, Y., Riasuti, R., Kaban, A. (2025). Development of a preliminary model for addressing naphthenic acid corrosion of ASTM A-335 P9 using an eco-enzyme green inhibitor on heavy-vacuum gas oil residue. Eastern-European Journal of Enterprise Technologies, 6 (6 (138)), 28–41. https://doi.org/10.15587/1729-4061.2025.347916*

1. Introduction

The refinery industry is renowned as a vital sector of the global energy supply, producing gasoline, diesel, jet fuel, liquid petroleum gas (LPG), heavy oil, kerosene, and naphtha from crude oil. In this sense, the conversion process comprises separation, conversion, and blending or treatments to meet the standard specification, including quality, safety [1, 2], environmental protection [3], and process control [4]. A typical refinery's economic system involves purchasing crude oil and selling products to maximize profit margins, despite the risk of acquiring sourer crude with higher sulfur content and total acid number (TAN) at an affordable price [5]. This activity aims to balance the risk of corrosion against production costs by implementing stricter and potent corrosion prevention measures on metallic materials, including those in the heavy gas oil (HVGO) piping system. The report shows that the risk of corrosion reaches 5% of the national gross national product [6] and poses environmental and business loss. Given the immense financial and non-financial losses associated with hydrocarbon delivery, it is imperative for refiners to ensure the safety and reliability of metallic materials to prevent catastrophic failures, such as oil spills and explosions [7]. Therefore, it is paramount to integrate corrosion mitigation and prevention to ensure reliable operation, operational flexibility, and cost-efficiency.

Naphthenic acid corrosion (NAC) corresponds to the high-temperature corrosion that occurs in distillation columns, where acid evaporates at elevated temperatures before

condensing on the lower-temperature wall of the column in the crude distillation unit [8]. The acid is classified as an aliphatic organic carboxylic acid with various cyclopentane or cyclohexane rings [9]. In short, the naphthenic acid has a general chemical formula of $C_nH_{2n-Y}O_2$, where n refers to the number of carbon atoms and y is attributed to the number of homologous series [10]. Naphthenic acid can be found in crude oil at nearly 4 wt% and acts as a corrosion-inducing contaminant; its severity primarily increases when the operating temperature reaches 400°C. Thereby, it requires intensive incentive to recover the material from NAC, mainly carbon steel.

A chromium-molybdenum ferritic alloy classified as ASTM A335 Grade P9 is among the most prevalent piping materials used for conveying atmospheric and vacuum residual hydrocarbons from the crude distillation unit before hydrocarbon processing and cracking. Hereafter, ASTM A335 Grade P9 will be referred to as the P9 material. Due to its well-balanced mechanical strength, thermal stability, and oxidation resistance, the P9 material is deemed suitable for piping in heavy vacuum gas oil (HVGO) services. In this context, the combination of Chromium (maximum 10%) and Molybdenum (maximum 1.1%) imparts superior strength, creep resistance, and oxidation protection when employed in HVGO lines.

Despite possessing the above mechanical and chemical properties, the P9 pipe often experiences mechanical degradation in the HVGO system. It is essential to note that five factors drive the susceptibility of P9 material against corrosion:

a) material composition;
b) sulfur content;
c) temperature;
d) naphthenic acid content;
e) wall shear stress [8].

The researcher in [11] demonstrates that 5Cr-½Mo steels exhibit greater corrosion resistance against NAC than Q235 when simulated at temperatures above 230°C. This was attributed to the higher activation energy at 5Cr-1/2 Mo (63.2 kJ/mol), which is more pronounced than that of Q235 (54 kJ/mol), indicating that higher temperatures accelerate the NAC corrosion rate. A notable work by [12] investigates the microstructure of SA210 C and A335-P5 steel at elevated temperatures and flushing angles, examining the material's response to the NA environment. The study reveals that the corrosion process initiates at the grain boundary, progressing towards the inner grain, where the ferrite corrodes.

Further supporting this fact, the paper of [12] reveals that the addition of Molybdenum (Mo) allows higher resistance of Mo-bearing against NAC, only when the amount of Mo reaches 0.7 wt. %. The anti-corrosion effect corresponds to the formation of a Mo surface film, which enhances the material's microstructure and microhardness. In addition, the scholarly teams of [13] shows the polyoxyethylene (n) mono oleate with various number of olate of 20, 40, and 80 as inhibitor in battling naphthenic acid corrosion on carbon steel. They found the carbon steel passivation can only be achieved due to formation and precipitation of oxide film where the less number of olate increases the inhibition efficiency and to adhere to Frumkin isotherm thermodynamic model.

Therefore, research on the development of inhibitors in battling the NAC is relevant to dive into a better understanding how to protect the downstream system of refinery unit against high temperature corrosion.

2. Literature review and problem statement

The paper [14] discusses managing the poison in the HVGO piping system by controlling catalyst use at the downstream site. It demonstrates that deasphalting can reduce asphaltene content in heavy crude oil and improve refining efficiency through solvent extraction with non-polar n-heptane, leading to better API gravity and pour point [15]. Despite extensive research, the influence of API gravity and pour point on crude oil properties has been documented; however, the performance of corrosion inhibitors in understanding inhibitor adsorption and their efficiency has not been systematically evaluated studied.

Another study [16], highlights the compatibility issues between gas hydrate and corrosion inhibitors caused by their chemical structures. They propose using an oleic acid-based anti-agglomerate inhibitor to prevent plugging. However, there is a limitation in understanding the functionality and compatibility of using green corrosion inhibitor outside of hydrate-forming conditions. In this case, a more environmentally friendly inhibitor is selected to close the gap research.

Additionally, [17] explores the use of biomass as an environmentally friendly corrosion inhibitor, reviewing various studies and emphasizing enhanced physical and chemical adsorption to form a stronger protective film. Nevertheless, it remains essential to develop a more comprehensive report that explores the utilization of peel-off fruits and vegetables and their preparation as base materials for inhibitor solutions. In this context, it pertains to environmentally friendly inhibitors derived from natural resources, while maintaining the costs and funding for inhibitor production at a relatively affordable level.

In contrast, the study in [18] demonstrates how to prepare a green corrosion inhibitor based on extraction method using White tea and details their preparation method. The researcher shows that extracting the inhibitor with acetone reduces corrosion in 1M HCl solution. Their findings indicate that the White tea inhibitor is highly effective, achieving nearly 95% inhibition efficiency. Although the influence of catechin in white tea has been studied for reducing corrosion at low pH, a comprehensive investigation of phenolic and aromatic compounds and their role in preventing pitting corrosion has not been thoroughly conducted, particularly when using a fermentation-based inhibitor solution. This area is often overlooked in recent research and remains insufficiently explored.

Additionally, the study in [19] highlights advances in scientific techniques for investigating the use of Syzygium Cumini leaf extract under similar conditions. They employ various spectroscopy methods, including Fourier-infrared spectroscopy (FTIR), potentiodynamic polarization (PDP), and electrochemical impedance spectroscopy (EIS), to assess the inhibitor's adsorption behavior. This results in a 93% inhibition efficiency through the adsorption of C=C and C=O functional groups in API 5L Gr B. The researcher revealed recent findings indicating that the adsorption process is governed and becomes more feasible as the values of ΔG_{ads} and ΔH_{ads} are 18.41 kJ/mol and 58.93 kJ/mol, respectively, to demonstrate the physical adsorption of the inhibitor on the surface of API 5L steel.

In this instance, there is a lack of testing and comparison of the performance of fermentation-based corrosion inhibitors within heavy-vacuum gas oil systems, including their inhibition mechanisms. Notably, the interaction between active functional groups and metals, such as ASTM A-335 P9, remains inadequately understood. This deficiency exists because most green

corrosion inhibitors tend to fail when simulated at elevated temperatures.

However, unresolved questions remain regarding the preparation of the corrosion inhibitor, particularly concerning the compatibility between the environment and the inhibitor at high temperatures, especially within the HVGO piping system. This issue stems from the scarcity of inhibitors compatible with poor-quality, high-hydrocarbon streams, leading to mixing problems and instability that make related research efforts unfeasible. One potential solution to these challenges is the discovery of several biomass-based inhibitors that are suitable for high-temperature conditions and are chemically stable when adsorbed onto the surface of metals, including chrome-molybdenum materials like ASTM A-335 P9. All this enables to assert that it is appropriate to undertake a study dedicated to the utilization of eco-enzymes derived from biomass or peel waste of fruits and vegetables, introduced as a promising candidate for corrosion prevention in heavy hydrocarbon streams, owing to their distinctive dual hydrophobic and hydrophilic properties, such as polyphenols and conjugated unsaturated C=C bonds.

3. The aim and objectives of the study

The aim of the study is to unveil the inherent potential of EE as a green corrosion inhibitor in the HVGO system under NA distillate environment.

To achieve this aim, the following objectives were accomplished:

– to analyze the chemical composition of materials used to assess their corrosion resistance;

– to identify the main functional groups responsible for inhibitor adsorption including the study of electronic transitions;

– to evaluate anti-corrosion activity through potentiodynamic polarization and electrochemical impedance spectroscopy;

– to determine the type of adsorption isotherm that explains the inhibitor's mechanism in preventing corrosion;

– to assess the changes in surface morphology caused by adsorption prior to and following the inhibitor's adsorption on the P9 steel surface.

4. Materials and methods

4. 1. Object and hypothesis of the study

In this work, the object of the study is ASTM A-335 P9 alloy where the same material was utilized as a common material for HVGO pipe. The prime selection of material due to a good balance between metallurgical and mechanical properties and resistance to sulfidation corrosion. In this case, the work models the P9 material's response to the risk of naphthenic acid corrosion by employing spectroscopic and corrosion tests, including a surface modification characterization test. This study utilized UV-Vis and FTIR spectroscopy to analyze electronic transitions and identify active functional groups. Furthermore, corrosion was investigated through potentiodynamic polarization and electrochemical impedance spectroscopy. Surface morphology was examined using SEM, and EDX was used to compare the surface condition of P9 metal before and after the addition of the inhibitor.

It is essential to acknowledge that eco-enzyme is proposed as a natural chemical agent to reduce the corrosion rate of P9 material and to facilitate the application of existing knowledge in assessing the inhibition mechanism at elevated temperatures. The presence of phenolic and aromatic compounds, as well as highly electronegative atoms such as oxygen, including electron delocalization, contributes to an increased level of inhibition by replacing water molecules in the vicinity of alloy P9. Furthermore, this study predicts that chemisorption surpasses physiosorption, owing to the abundance of phenolic and electron-donating oxygen atoms capable of establishing dative covalent bonds and hydrogen bonds. Access to this information enables effective adsorption strategies, thereby leveraging knowledge on how eco-enzymes protect P9 material from deterioration caused by corrosion.

4. 2. Preparation of the eco-enzyme inhibitor

The inhibitor was prepared by mixing twenty grams of various fruit and vegetable waste (kitchen waste) with molasses (brown sugar) and distilled water, in a ratio of 3:1:10, as modeled and pioneered by the work of [20], with slight improvement, such as providing the common polyphenol in vegetables and fruits. In this case, the molasses promotes microbial growth via various hydrolytic enzymes and is dissolved in the solvent (demineralized water), as depicted in Fig. 1.

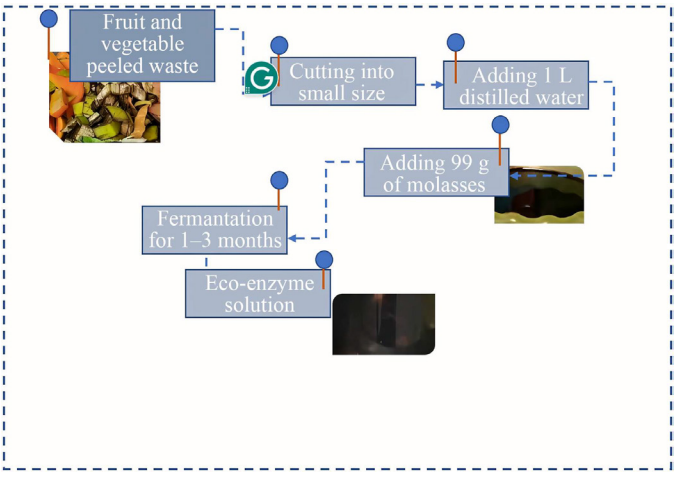

Fig. 1. The simplified step of the eco-enzyme preparation stage [20]

The final pH of EE was measured to determine whether an essential weak acid was present [21]. The fermentation process was allowed to run for 3 months to produce a final solution of 1000 dm^3 of the EE inhibitor.

4. 3. The preparation of the test solution

In this work, a blank solution was an aqueous electrolyte of crude oil collected at the HVGO residue outlet, which was heated to nearly 400°C before being collected for laboratory functional group identification (Fig. 2).

The blank solution was prepared by adding a mild electrolyte to promote the corrosion process, producing naphthenic acid (NA) distillate, despite its role in increasing ionic conductivity. In this case, a 1 M solution of K_2SO_4 (Sigma-Aldrich) with a conductivity of 100 mS/cm was prepared, and all measurements were performed at room temperature to influence the acid partitioning between the oil and water phases. The addition of K_2SO_4 aims to control the amount of water and alter the acid extraction behavior, as reported in [21].

Fig. 2. The test solution

4. 3. Chemical composition test

The P9 material serves as the working electrode and is the object of the study before undergoing chemical composition analysis by optical emission spectroscopy (OES), performed with Bruker equipment. Chemical composition analysis was intended to determine the elemental composition of P9 alloy before releasing the quantities of the inspected elements, such as Fe, Cr, Ni, and Mo, that correspond to its corrosion resistance against naphthenic acid corrosion.

The sample was prepared with dimensions of 1 × 1 × 1 cm and immersed in a solution of HNO_3 and HCl. Additionally, OES was used to determine the elemental composition percentages of the material, which relate to its corrosion resistance against NA corrosion. The samples were exposed to a plasma power of 1.25 kW, with a gas flow of about 10 L/min of Argon and a nebulizer gas flow of 0.75 L/min.

4. 5. Functional group characterization and electronic transition

This study employed Fourier transform infrared (FTIR) spectroscopy, utilizing a PerkinElmer instrument, to identify the functional groups in the inhibitor and test solution. P9 steel samples were immersed in an 80 ppm EE inhibitor solution (NA extracts) for three days before being removed and dried under nitrogen gas. Additionally, the UH5300 Spectrophotometer UV-Vis spectroscopy with serial number 3048-010 was utilized to analyze the electronic transitions of the active compound in EE and to evaluate their adsorption onto P9 steel, both prior to and following simulated NAC with scan speed 200 nm/min using 6 auto cell mode.

Both the pure EE solution and the NAC solution, prepared at an optimal concentration with wavelengths ranging from 200 to 800 nm, were examined. The presence of phenolic, carbonyl, and symmetric C=C bonds, contingent upon the chemical composition, was presumed to augment the corrosion inhibition properties of P9 steel at 60°C.

4. 6. Electrochemical tests

The primary objective of the electrochemical testing is to elucidate the material's response to the inhibitor within an NA simulated environment across various concentrations and temperatures. The electrochemical analyses were conducted using a Metrohm Autolab with a PGSTAT 302N workstation, employing a conventional three-electrode setup. In this work, the operating principle comprises of working electrode, reference electrode, and auxiliary electrode. The typical instrument employs the voltage and current at 20V and 1 A.

The working electrode comprised P9 steel with an exposed surface area of 1 cm2 and was cleaned using Grit paper from # 60–1000. A saturated Ag/AgCl electrode served as the reference, while a platinum electrode functioned as the auxiliary. The procedure was embarked beginning with a sixty-minute open-circuit potential (OCP) test before conducting the electrochemical impedance spectroscopy (EIS) at the OCP spans the frequency at 0.01–105 Hz and the scan rate of 1 mV/s. Furthermore, the Tafel analysis was conducted using a potential range of –30 to 30 mV at a scan rate of 1 mV/s. The corrosion rate, Tafel slopes (βa and βc), corrosion current density (icorr), and corrosion potential (Ecorr) for both inhibited and non-inhibited systems were determined using Nova software. Moreover, the inhibition efficiency was calculated using Equation 1adheres to the ASTM G5 and was presented in equation (1) [22]

$$\eta\% = \frac{R_s - R_{inh}}{R_s} \times 100\%, \quad (1)$$

where R_s and R_{inh} – the charge-transfer resistance and EE film inhibitor resistance (Ω cm^2).

It is prime to note that the performance of the inhibitor was calculated by the capacitance of the double layer as depicted in equation (2) [23]

$$C_{dl} = [Y_0 \times \left\{ \exp\left[1/n\right] \times \exp\left[\frac{1-n}{n}\right] \times \left(\frac{R_s R_{inh}}{R_s + R_{inh}} \right) \right\}. \quad (2)$$

In the equation (2) Y_0, n, R_s, and R_{inh} represent system passivity, deviation index, solution resistance, and inhibitor resistance, respectively.

4. 7. Surface morphology studies

In this study, the cleaned P9 electrode was immersed in both inhibited and non-inhibited systems at their maximum concentration, then examined using a Scanning Electron Microscope (SEM) LEO Supra 50VP. The instrument utilizes a focused beam with high electron energy they generate a signal and form a surface topography image. The specimen was mounted with conductive silver adhesive tape before imaging, which was conducted with an electron gun set at an accelerating voltage of 15–20 kV and a current of 8 mA. The imaging process lasted fifteen minutes at a maximum magnification of 10,000x before the images were transferred to a computer.

5. Results of eco-enzyme as green corrosion inhibitor

5. 1. Chemical composition test

Table 1 shows the results of the chemical composition test linked to the corrosion resistance of the EE inhibitor against NAC.

Table 1

The optical emission result

C	Si	Cr	Mo	Co	N	Fe
0.080	0.481	9.135	0.894	0.01	0.01	88.76

The superior corrosion resistance of P9 results from the remarkable amounts of Cr (9.135%) and Mo (0.894%). In this case, the 9Cr-1Mo steel remains susceptible to NAC due to an

unstable Cr-oxide layer. On the contrary, the detection of Mo shows resistance to NAC despite the addition of Mo, which stabilizes corrosion resistance against NAC.

5. 2. Functional group identification and electronic transition

Fig. 3 illustrates the response of P9 steel to various absorption functional groups, which correspond to the formation of protective films and their associated complex compounds when the metal is exposed to a naphthenic acid environment.

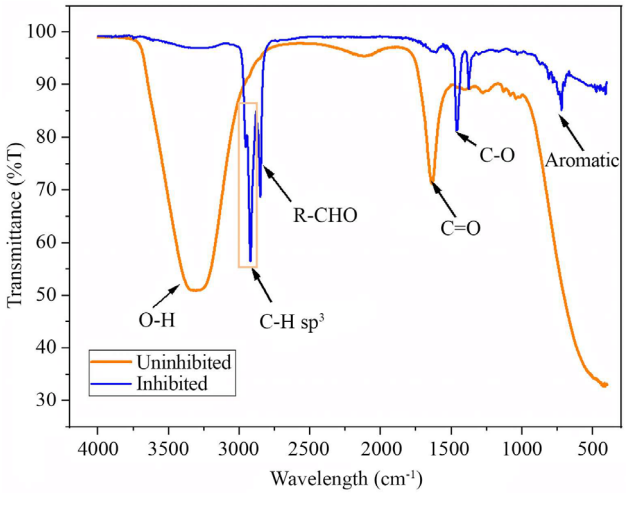

Fig. 3. The functional group identification test of eco-enzyme result both unhibited and inhibited P9 steel

The high anticorrosion activity is linked to their phenolic content. In this work, the wavelength spectrum of EE shows prominent peaks at 3200–3500 cm^{-1}, indicating the O-H stretch from phenol or alcohol groups. It is important to note that the O-H bond involves strong electron sharing, and stable resonance structures may exist before hydrogen bonding (Fe-O) forms [24].

The aromatic phenolic compound enables π-d interactions, resulting in effective adsorption and facilitating chemisorption, thereby enhancing film stability. Consequently, it is appropriate to permit the injection of EE inhibitor into HVGO lines.

Furthermore, the presence of C-H sp^3 bonds is evident in the wavelength range of 2800–3000 cm^{-1} to provide a physical barrier and reduce water and corrosive contact with metal [25]. In this case, the hydrophobic character facilitates the water-repellent system when the inhibitor is injected into HVGO lines.

The detection of R-CHO at around 2600–2700 cm^{-1} indicates the availability of highly electronegative oxygen atoms capable of donating electron pairs to Fe^{2+} ions in the P9 material [26]. In this context, the polarized carbonyl groups participate in the formation of surface complexes, wherein the presence of electropositive hydrogen enhances their reactivity, facilitating inhibitor adsorption and increasing surface binding. Moreover, the inhibited system shows the C=O peak at 1600–1700 cm^{-1} which is associated with the formation of a stable chelate ring with metal ions, possibly increasing inhibitor adsorption strength. This allows the π-bond in the carbonyl group to donate electrons into the vacant d-orbitals of the iron atom, thereby strengthening the protective layer against corrosion.

Additionally, the C-O single bond at 1400–1500 cm^{-1} shows additional electron-donating behavior indicating that the inhibitor adheres to the P9 surface by stabilizing the oxygen dipole and metal interaction [27]. This occurs due to the formation of a coordination bond, which remains weaker in comparison to the C=O bond of Fe.

Furthermore, it is crucial to demonstrate that the contribution of an aromatic ring, such as benzene, at approximately 700 cm^{-1} indicates the π-electron cloud interaction with Fe d-orbitals and enhances π-π interactions. This correlates with the potential formation of strong physisorption or chemisorption, thereby confirming the presence of phenolic groups. In this context, the aromatic ring increases the proximity of the inhibitor molecule to the metal surface, facilitating a stronger planar adsorption within their monolayer structure.

Moreover, Fig. 4 shows various functional group of pure EE inhibitor at their various wavelength and electronic transitions.

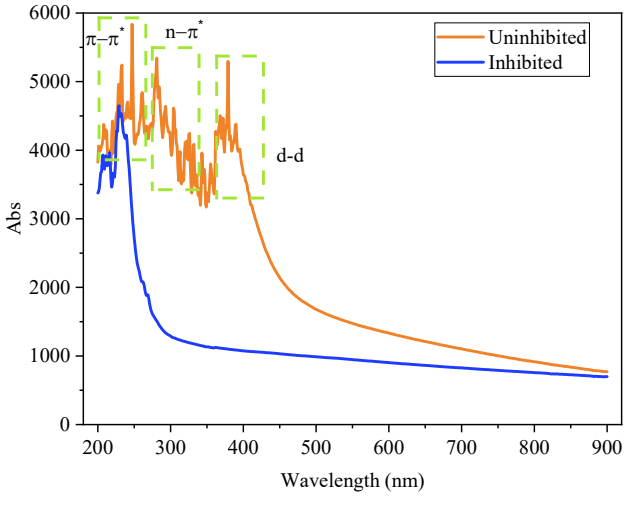

Fig. 4. The ultraviolet identification result of actual inhibitor

Fig. 4 illustrates the characteristics of the inhibitor within both the inhibited and uninhibited systems when immersed in an eco-enzyme solution at a concentration of 80 ppm after several days of immersion. It is evident that the inhibited system exhibits lower absorbance, as well as shifts and suppression of characteristic peaks, indicative of a robust interaction between the EE inhibitor and the P9 surface or their corresponding ions. Notably, the fluctuations in UV absorption within the range of 200–250 nm correspond to the π-π* transition of aromatic rings (benzene), aligning with the FTIR result at 700 cm^{-1} (Fig. 4). Additionally, these fluctuations involve the conjugated π system of C=C and C=O, where π electrons participate in the adsorption process. Furthermore, the n-π* transition is attributed to the lone pair electrons of oxygen atoms, evidenced by a peak within the 250–300 nm range. The faint tail observed around 300–350 nm suggests the presence of conjugated carbonyl groups, demonstrating both π-π* and n-π* transitions, thereby indicating the amphipathic nature – comprising both hydrophobic and hydrophilic characteristics – of the EE inhibitor [28]. Moreover, the conjugated -CH=CH- group, extending approximately from 300 to 400 nm, supports the hypothesis that the EE inhibitor possesses an enhanced capacity for metal-to-ligand charge transfer [29]. The d-d transition is observable at the peak, approximately between 350–400 nm, in the uninhibited system, despite its diminished appearance in the inhibited system. The disappearance of this peak aligns with the reduced absorbance

observed in the inhibited system. Ultimately, the broad visible tail extending beyond 400 nm indicates extended conjugation of the d-d orbital, which is consistent with the presence of a conjugated polyene functional group.

5. 3. Electrochemical test results

Fig. 5 shows the open circuit potential (OCP) of a blank test solution at various temperatures, highlighting the shift in natural electrochemical potential after adding the inhibitor.

Fig. 5, *a* illustrates that the sole OCP of the uninhibited (blank) solution at various temperatures shifts towards a positive value from −0.34 V to −0.26 V over the period from 0 to 1800 seconds. The fluctuation graphs confirm the instability of the protective layer of P9 steel, which may correspond to localized corrosion. It is also evident that the protective chromium oxide layer begins to deteriorate at temperatures exceeding 40°C, as indicated by a noticeable decrease in potential from approximately −0.26 V to −0.28 V. In contrast, the plateau observed at 25°C in the inhibited system suggests the formation of a continuous protective film of EE inhibitor on the surface of P9 steel. However, as temperature increases, the stability of the passive layer decreases, despite potential shifts towards a more positive potential at approximately −0.20 V at 40°C and 60°C.

It is also noteworthy that the rapid shifts indicate accelerated adsorption of the EE inhibitor on the P9 steel. Fig. 6, *a* shows the potentiodynamic polarization measurements for both uninhibited and inhibited samples of EE in the NA extract solution.

Fig. 6, *a*, displays the Tafel Polarization trend for different inhibitor concentrations measured at 60°C. In this case, the Tafel curves illustrate the corrosion-inhibitory properties of the EE inhibitor in the NA distillate. The cathode branch for all inhibitor concentrations remains parallel to that of the blank solution. Similarly, the anodic branch shows significant shape changes, particularly at 80 ppm.

Furthermore, the principal parameters derived from the graph include the corrosion potential (E_{corr}), corrosion current density (i_{corr}), anodic slope (β_a), and cathodic slope (β_c). In this context, the calculation of inhibition efficiency is presented in equation (3) [29]

$$\eta(\%) = \frac{CR_{blank} - CR_{inh}}{CR_{inh}} \times 100\%. \quad (3)$$

In this case, the CR_{blank} and CR_{inh} correspond to the corrosion rate of the blank and the inhibitor solution (mmpy) and their calculation is given in Table 2.

Table 2

The potentiodynamic polarization parameters for P9 material under NA distillate with and without the existence of EE inhibitor

Solution (ppm)	Temperature (K)	*Ba* (mV/decade)	*βc* (mV/decade)	i_{corr} (μA/cm^2)	E_{corr} (V vs. SCE)	Corrosion Rate (mmpy)	Inhibition efficiency (%)
Blank	298	0.0167	0.0149	7.4542	−0.3395	0.0086	0
Blank	313	0.0143	0.0191	1.9289	−0.25744	0.0224	0
Blank	333	0.0181	0.0146	5.4512	−0.26554	0.0063	0
20	298	0.0151	0.0161	2.6649	−0.36262	0.0039	54.62
20	313	0.0157	0.0155	3.2787	−0.3823	0.0040	81.97
20	333	0.0197	0.0163	7.3787	−0.29441	0.0047	25.32
40	298	0.0196	0.0177	3.4776	−0.377	0.0032	62.47
40	313	0.0210	0.0207	4.3366	−0.30551	0.0085	61.76
40	333	0.0208	0.0260	5.7938	−0.24848	0.0008	86.21
80	298	0.0134	0.0160	2.6758	−0.36261	0.0031	64.21
80	313	0.0169	0.0171	5.7098	−0.32844	0.0066	70.42
80	333	0.0255	0.0125	2.7988	−0.20003	0.00054	92.04

It is also important to note that as concentration increases, the cathodic branch of the overall concentration remains in parallel. In contrast, the anodic and cathodic branches exhibit significant changes, particularly for the 80 ppm EE solution (Fig. 6, *a*). The shift in log*i* toward more negative values aligns well with the results in Table 2, indicating that double protection decreases corrosive activity and slows P9 degradation.

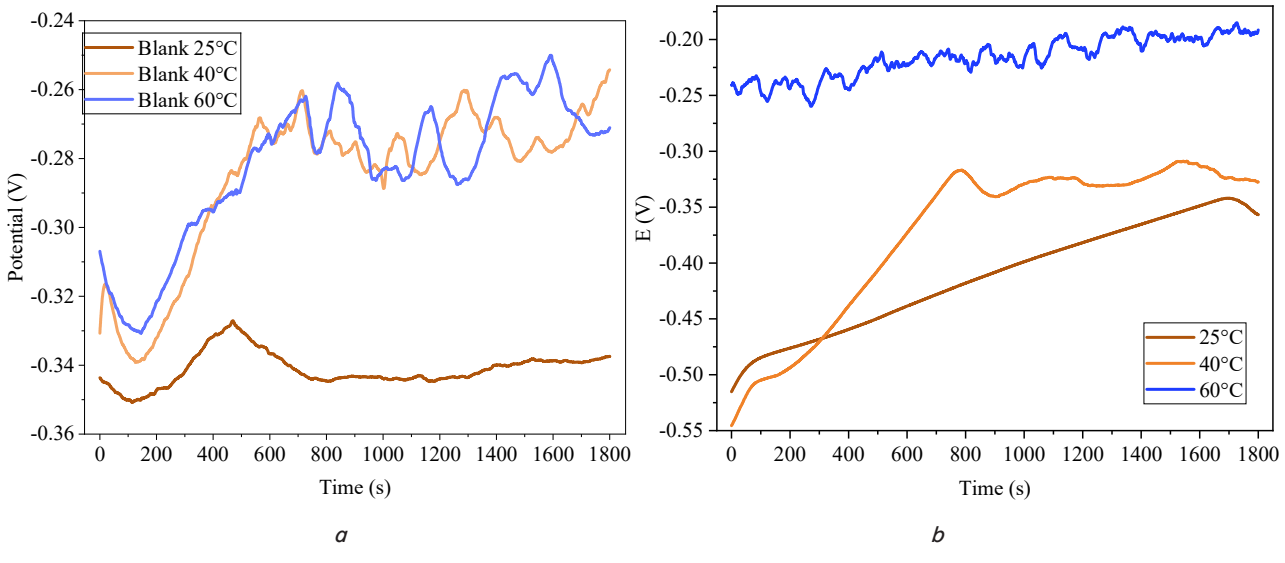

a *b*

Fig. 5. The open circuit potential of: *a* — blank; *b* — 80 ppm at various temperatures

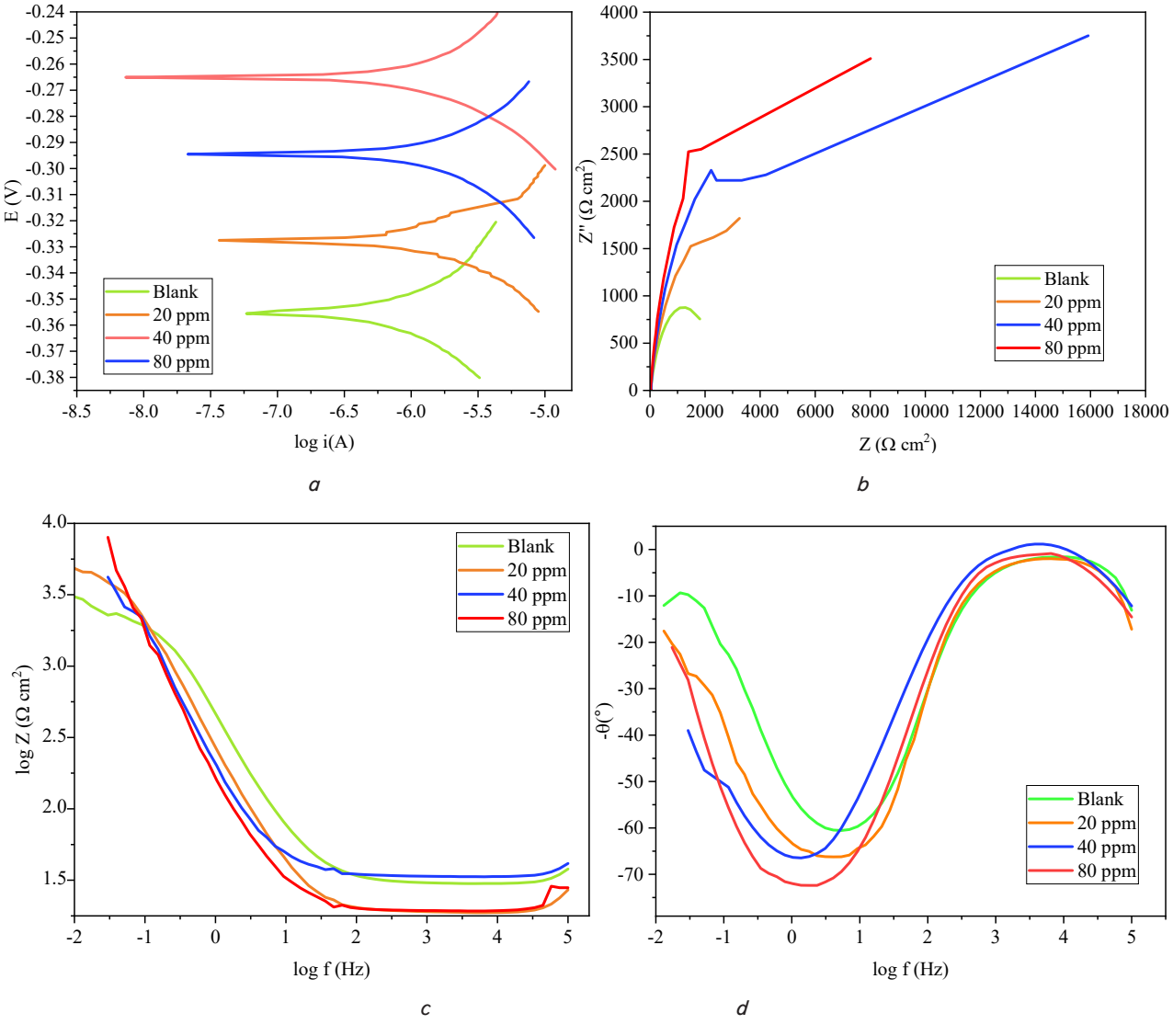

Fig. 6. The corrosion test results: *a* — Tafel plot; *b* — Nyquist plot; *c* — Bode plot; *d* — Bode modulus plot at 60°C

Fig. 6, *b* illustrates the Electrochemical Impedance Spectroscopy (EIS) test, which provides insight into the interaction between the metals and the EE inhibitor, including an analysis of the corrosion inhibitor's performance. It is important to note that the Nyquist plot shows an increase in the semicircle diameter for the EE inhibitor at 60°C, from the blank solution to 80 ppm. The center of the semicircle lies on the real axis, indicating that a charge-transfer process has occurred [30]. It is also clear that as the concentration of the EE inhibitor increases, its inhibitory capacity increases.

Table 3 presents the data for R_{ct}, R_{inh}, *CPE* (Y_0 and n), and inhibition efficiency across various concentrations and temperatures, attributed to charge transfer resistance, inhibitor resistance, and the constant phase element (CPE). It is evident that the drop in R_{ct} from 29.8 Ω to 19.6 Ω indicates faster electron transfer, which induces the corrosion process. On the other hand, the rise of R_{inh} corresponds to the rapid formation of an inhibitor film (passive layer) from 1680 Ω to 7430 Ω. In this work, the *CPE* value agrees with the passivation of metal, and (4) shows the Y_0 calculation [31]

$$Z_{CPE} = \frac{1}{(Y_0)(j\omega)^n}. \quad (4)$$

Table 3

Electrochemical impedance parameters of P9 steel under NA extracts

Conc (ppm)	Temp (K)	*Rs* (Ohm)	R_{inh} (Ohm)	*CPE*		Inhibition efficiency (%)
				Yo ($\times 10^{-6}$ Ω^{-1} cm^{-2Sn})	*n*	
Blank	298	58.4	1250	0.0282	0.947	0
Blank	314	30.7	1400	8.47	0.778	0
Blank	333	29.8	1680	18.7	0.927	0
20	298	29.8	2350	0.54	1	46.80
20	314	43.9	2540	6.1	0.767	44.88
20	333	26.5	2570	6.18	0.88	34.63
40	298	60.2	2870	2.93	0.811	56.44
40	314	43.2	3700	5.59	0.744	62.16
40	333	20.4	3850	4.65	0.763	56.36
80	298	76.5	7310	7.78	0.721	82.90
80	314	31.4	6610	5.58	0.774	78.81
80	333	39.6	7430	3.82	0.702	77.38

In the equation (4) *j*, ω, and *n* are imaginary root, angular frequency, and deviation index.

Furthermore, it is essential to derive the value of n from Table 3. Based on [32], the range value of n spans from –1 to 1. When $n = -1$, the CPE acts as a conductor; at $n = 0$, it represents Warburg Impedance; and at $n = 1$, the CPE shows pure capacitive behavior. In this study, the decrease in n from 0.927 to 0.702 suggests greater heterogeneity in the adsorption of the inhibitor on the P9 surface as the temperature increases to 60°C, thereby facilitating the formation of a thicker film on the P9 steel.

The decline in the value of Y_0 at 60°C is observed from 18.7 to 3.82 $\Omega^{-1}cm^2$. S^n indicates the displacement of water molecules through the formation of EE inhibitors. Fig. 6, *b* shows the Nyquist graph of various concentrations measured at 60°C. It is clear that the increase in Nyquist semicircle diameter corresponds to the passivation state and increases the resistivity of P9 material against acidic NA distillate. In this case, the shorter irregular semi arc in the blank solution shows a distinct effect on electron transfer. In contrast, the diameter increases with increasing concentration (20, 40, and 80 ppm), where the impedance is nearly 1400 Ω cm^2. However, the impedance at 40 ppm is more noticeable than that at 80 ppm and extends its radius (Fig. 6, *b*).

A similar observation is noted for the Bode plot and the Bode modules at various concentrations, and their behavior is perfectly fit to the electrical equivalent diagram depicted in Fig. 7.

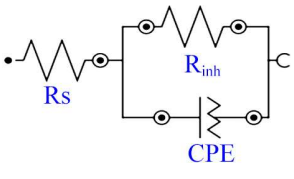

Fig. 7. The electrical equivalent diagram

In addition, the Bode and Nyquist plots indicate that physical corrosion control is achieved at 60°C. As concentration increases, both impedance (log |Z|) and phase angle change. Specifically, the impedance at low frequencies for the blank solution to 80 ppm demonstrates an increasing trend from 3.5 to 3.8 Ω·cm^2. Despite the rise in impedance, the overall impedance of the inhibited system decreases from 1.6 to 1.4 Ω·cm^2. The presence of a twin-wide shoulder on the Bode phase (Fig. 6, *d*) aligns well with the capacitive loop observed in the Nyquist plot.

At low frequencies, the phase angle of the EE inhibitor at 80 ppm approaches 90°, indicating predominantly capacitive behavior, whereas the more negative phase angles, ranging from 60° to –85°, indicate stronger capacitive behavior. Additionally, phase angles between –10° and –30° indicate the inhibitor's resistive nature.

5. 4. Adsorption isotherm of inhibition

Table 4 presents the thermodynamic parameters of the EE inhibitor, which are essential for understanding the nature of inhibitor adsorption across different concentrations and temperatures.

The pair of K_{ads} (equilibrium constants for adsorption and desorption of the inhibitor) and ΔG_{ads} govern the stability of the passive film. In this instance, it is evident that the value of K_{ads} increases from 20 to 80 ppm, from 0.0264 to 0.042 L mol^{-1}. The calculation of ΔG_{ads} of the inhibited system is given in equation (5)

$$\Delta G_{ads} = -RT \ln\left(1\times10^6 K_{ads}\right). \quad (5)$$

Table 4

The thermodynamic parameter of the EE inhibitor

Conc (ppm)	Temp (K)	Surface coverage (θ)	K_{ads} (L mol^{-1})	ΔH_{ads} (kJ/mol)	ΔS_{ads} (kJ/mol)	ΔG_{ads} (kJ/mol)
20	298	0.4680	0.0440	15.2940	140.2176	–26.4901
20	314	0.4488	0.0407	16.5779	139.5724	–28.504
20	333	0.3463	0.0275	17.0912	135.9983	–28.1963
40	298	0.5644	0.0324	12.7980	129.2920	–25.7318
40	314	0.6216	0.0410	13.8707	131.2637	–28.5274
40	333	0.5636	0.0333	14.3001	129.2641	–28.7448
80	298	0.8290	0.0536	23.9163	170.7895	–26.979
80	314	0.7882	0.0527	25.9227	170.6595	–29.2004
80	333	0.7738	0.0427	26.7252	168.9155	–29.5236

In this case, R and T denote the gas constant, 8.314 J/K, and the absolute temperature in Kelvin, respectively. According to Table 4, the calculated ΔG_{ads} at 80 ppm and 60°C is –29.5236 kJ/mol, indicating the chemisorption adsorption characteristic of the EE inhibitor [33]. Furthermore, the enthalpy change of adsorption can be determined through the application of equation (6) [34]

$$\ln K_{ads} = -\frac{\Delta H_{ads}}{RT} + k_2. \quad (6)$$

It is possible to note that the ΔH_{ads} measured at the same condition is +26.72521 kJ/mol. In this work, the calculated value of ΔH_{ads} is consistent with the calculated value of ΔG_{ads} through the chemical means due to their values falling within the range of 15–26 kJ/mol based on the publication of [35]. Eventually, the calculated entropy adsorption has been directly linked to the organization of the inhibitor when the EE inhibitor adsorbs onto the P9 steel and is depicted in equation (7)

$$\Delta S_{ads} = \frac{\Delta H_{ads} - \Delta G_{ads}}{\Delta T}. \quad (7)$$

It is generally acknowledged that the increase in entropy value from 135.9983 kJ/mol to 168.9155 kJ/mol indicates the thermal stability and the irreversible process involved in the formation of the passive layer EE inhibitor at 60°C.

Moreover, it is critical to determine the type of EE inhibitor adsorption by analyzing the isotherm using equation (8)

$$\frac{C_{inh}}{\theta} = \frac{1}{K_{ads}} + C_{inh}. \quad (8)$$

In the aforementioned equation, θ represents the surface coverage area of the inhibitor protection. It is important to note that as the concentration and temperature increase, the inhibition effectiveness exceeds 100% (rising from 0.346304 to 0.77389), indicating that the inhibitor effectively forms a protective layer at higher temperatures. In this case, the plotting C_{inh}/θ versus $1/K_{ads}$ yields an R^2 value that corresponds to the type of inhibitor adsorption model describing how the eco-enzyme inhibitor interacts with P9 steel at constant temperature. Based on the R^2 calculation, the adsorption isotherm follows the Langmuir isotherm for an inhibitor concentration of 80 ppm at 60°C.

Table 5

The calculated R^2 of EE inhibitor

Concentration (ppm)	R^2
20	0.9183
40	0.84975
80	0.8537

Table 5 indicates that the proximity of R^2 to 1 corroborates the applicability of the Langmuir adsorption model in elucidating the formation of a single passive layer on the surface of P9 steel [36].

5. 5. Surface morphology studies

Fig. 8 compares and contrasts the surface morphologies of the P9 material when immersed in an inhibitor and a non-inhibitor system to reveal the corrosion protection of the EE inhibitor.

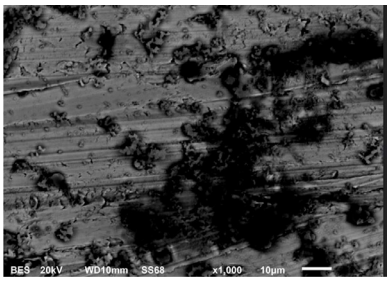

a

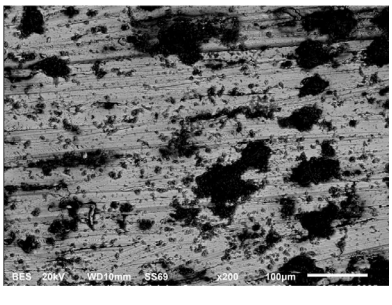

b

Fig. 8. The scanning electron microscope result of: *a* — uninhibited; *b* — inhibited system

It is important to note that the rough surface of P9 prior to inhibitor injection features irregular pits and rounded areas, with clear corrosion products, especially in several regions, due to exposure of P9 steel to the NA distillate solution (Fig. 8, *a*). In this context, the surface morphology is characterized by a low K_{ads} value, indicating that the P9 material exhibits a high degree of micro-roughness. This is indicative of potential film instability.

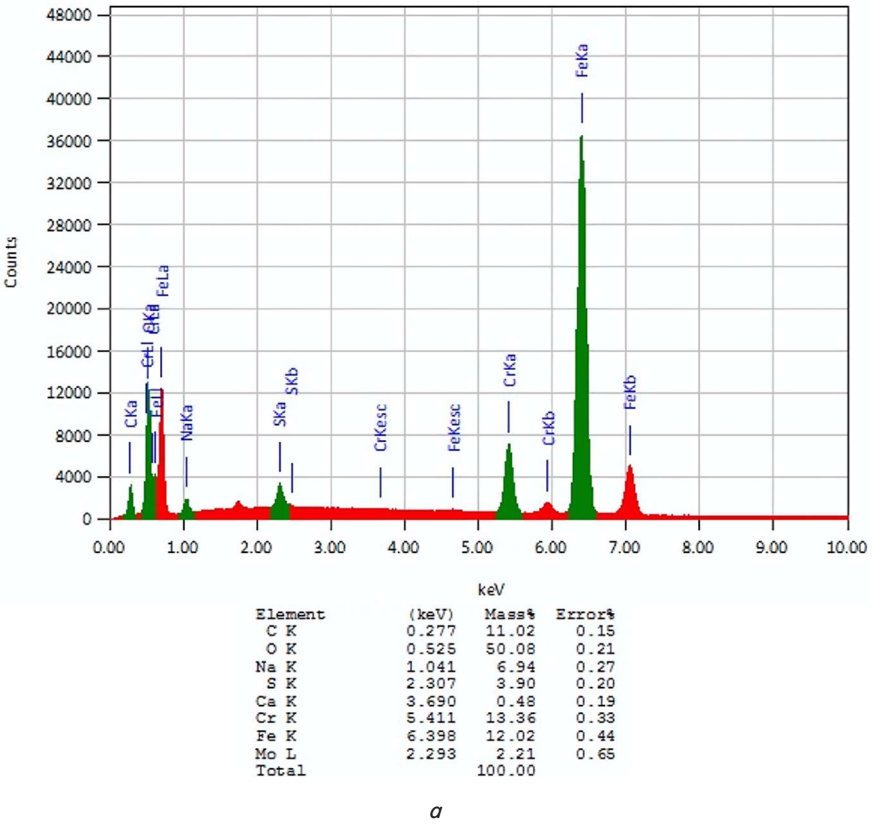

Element	(keV)	Mass%	Error%
C K	0.277	11.02	0.15
O K	0.525	50.08	0.21
Na K	1.041	6.94	0.27
S K	2.307	3.90	0.20
Ca K	3.690	0.48	0.19
Cr K	5.411	13.36	0.33
Fe K	6.398	12.02	0.44
Mo L	2.293	2.21	0.65
Total		100.00	

a

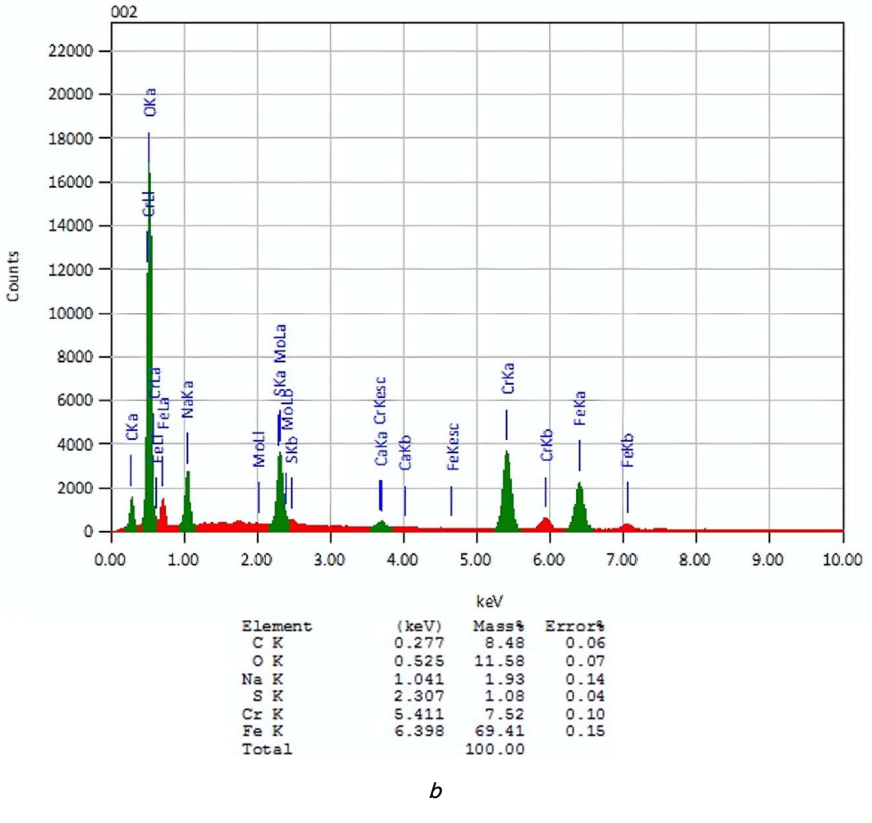

Element	(keV)	Mass%	Error%
C K	0.277	8.48	0.06
O K	0.525	11.58	0.07
Na K	1.041	1.93	0.14
S K	2.307	1.08	0.04
Cr K	5.411	7.52	0.10
Fe K	6.398	69.41	0.15
Total		100.00	

b

Fig. 9. The energy dispersive X-ray-results of: *a* — uninhibited; *b* — inhibited System

On the contrary, upon addition of the inhibitor, the surface of P9 steel has increased in its surface roughness, where the number of pits decreases moderately due to the adsorp-

tion of the inhibitor. In this case, the higher value of θ and K_{ads} at 0.77389 L mol^{-1} and 0.042783.

It is evident that the high mass fractions of oxygen and sulfur, at 50 wt.% and 3.90 wt.% respectively, are accompanied by a comparatively lower Fe content of 12.02 wt.%. In this case, the presence of S confirms the formation of FeS formation on the surface of P9 that has inhibiting effect towards NAC.

As expected, the reduction of sulfur content in the inhibited system to 1.93 wt.% confirms the presence of naphthenic acids, which corresponds to the removal of iron sulfide scales on the P9 steels. Accordingly, the decrease in oxygen content from 50.08 wt.% to 11.58 wt.% indicates a significant reduction in the corroded layer and the formation of a single thick layer, consistent with the Langmuir adsorption isotherm model. This justifies the high R_{inh} value and the inhibition efficiency. Furthermore, the decrease in Chromium content from 13.36 wt.% to 7.52 wt.% corresponds to the formation of Chromium oxide under the elevated-temperature conditions of P9 steel during the corrosion assessment.

6. Discussion of eco-enzyme as a green corrosion inhibitor

This study explores and models the novel corrosion protection of P9 material to defend against naphthenic acid corrosion, using an eco-friendly enzyme-based green corrosion inhibitor. The currently used commercial inhibitor has been identified as toxic to hydrotreating and hydrocracking units in fluid catalytic cracking, mainly due to its phosphorus, nitrogen, and sulfur content. Phosphorus can hinder hydrogenation, while nitrogen and sulfur may cause issues like acid blockage, reducing catalyst lifespan in downstream units. Additionally, the existing catalyst remains environmentally toxic.

In this study, EE was employed as a corrosion inhibitor by adjusting the process temperature and concentrations, with P9 material tested under the NA extract. The material conformity test results demonstrate that the material complies with the P9 specifications. As shown in Table 1, the material exhibits compatibility and corrosion resistance, attributable to the formation of a stable Cr oxide layer. This observation aligns with the report of [28], which characterizes corrosion resistance as facilitated by normalization and tempering processes that develop a ferritic-martensitic microstructure at elevated temperatures. In this sense, the stability of the oxide layer is a key factor in enabling corrosion resistance. Furthermore, this investigation is essential to address the inadequacy of P9 material in forming a stable protective chromium oxide layer, particularly due to the presence of naphthenic acids. In this context, the dissolution of iron by naphthenic acid results in material loss, as the P9 material cannot achieve self-passivation in naphthenic acid environments. This process involves the formation of weak oxide films and necessitates the use of artificial passivation inhibitors to safeguard the surface.

Moreover, the UV-Vis results are consistent with the FTIR results, where the dominant functional groups are aromatic -OH, C=O, conjugated C=O, -CH=CH-, and C-O, which promote the adsorption of the EE inhibitor to the metallic surface. As outlined in Fig. 4, the presence of a UV-absorption peak at 200-250 nm corresponds with the presence of aromatic rings, C=C, and C=O (conjugated π-system). In the inhibited system, the π electron is donated to the d-orbital of Fe to form a complex compound while minimizing the free electronic transition. The π-π* shows the presence of aromatic rings and C=C double bond in EE inhibitors, where the molecules are responsible for providing delocalized electrons to donate to iron ions. In this case, the Fe atom from the P9 material becomes the electron acceptor. Furthermore, the conjugated C=O and electron-rich functional groups stabilize the adsorption process due to active donation of electrons to the vacant d-orbital of Fe before they form the Fe-inhibitor complexes. In addition, indicating that the inhibitor adheres to the P9 surface by stabilizing the oxygen dipole and metal interaction. This result is comparable to the finding of [37], where the dipole-dipole moment contributes to the more substantial electron donation to the metal ion.

Moreover, the n-π* transition indicates the potential for the lone pair electrons of oxygen to participate in coordinate bonding with Fe^{2+}, thereby demonstrating the interaction between the inhibitor and the metal. The reduced absorbance observed in the inhibited system at 300–350 nm suggests that the inhibitor partitions between the oil and water layers. Furthermore, the metal-to-ligand charge transfer reflects structural changes in the EE inhibitor. At the same time, the extension peak at 350–400 nm is believed to confirm the chemisorption process of EE via a donor-acceptor mechanism.

It is essential to note that FTIR results confirm the composition of the organic compound, which may interact with the P9 surface both physically and chemically. This interaction increases the coverage of the affected surface due to corrosion, forming a thin protective layer that shields the P9 surface from aggressive ions in a naphthenic acid environment. The disappearance of specific peaks from the uninhibited to the inhibited system provides evidence that the EE solution effectively protects P9 steel. The presence of aromatic and phenolic structures, as well as electron-rich groups such as -OH, RCHO, and C=O, and electronegative oxygen atoms within EE molecules, is attributed to its effective inhibition performance [38].

Based on Fig. 5, the appearance of 200-400 nm specifically shows the conjugated system due to the presence of polyphenols and confirms the EE FTIR result. Also, it is clear that the aromatic band around 700 cm^{-1} is in good agreement with the π-π* transition, while the n-π* transition reveals the presence of C=O and hydroxyl (O-H). A few changes in the spectrum have been observed in the inhibited system, indicating adsorption of the EE inhibitor, compared to the non-inhibited system, where the spectrum shows higher absorbance [39]. Additionally, the presence of various functional groups affects the quantitative corrosion measurement through the implementation of corrosion tests (potentiodynamic and EIS).

Based on the Tafel plot, a consistent trend is observed in both the anodic and cathodic branches across various concentrations at 60°C. It is apparent that the anodic and cathodic Tafel curves shift concurrently, indicating a reduction in the corrosion rate and suggesting the presence of a mixed-type inhibitor. This is further corroborated by the observed shift in the corrosion potential (E_{corr}) by approximately ±0.085 V before and after the addition of the inhibitor EE to the system (Table 2) [40]. Additionally, the anodic branches in the inhibitor-containing system shift to lower current densities at approximately 2.7988 A (Table 2), implying that the inhibitor diminishes the oxidation process of P9 and reduces the conversion of Fe to Fe^{2+} ions. Notably, the linear regions at 40 and 80 ppm clearly demonstrate that

the inhibitor effectively controls electron transfer. The passivation regions are identified at the same concentrations at relatively elevated potentials near -0.3 V, indicating that the corrosion current density remains comparatively low despite more negative E_{corr} values. This suggests that P9 steel exhibits a broader passivation region and a stable passive film [41]. According to Fig. 6, *a*, the Tafel graphs show at least three regions: the linear, plateau, and no-inhibition zones. In this context, the uninhibited solution resides within the no-corrosion-inhibitor zone due to the low potential and minimal anodic current density. As the concentration increases, the curves at 20 and 40 ppm reveal a corrosion-inhibitor region where the relationship between corrosion current density and potential is linear. Furthermore, it is noteworthy that rising the concentration from 40 ppm to 80 ppm at 333 K results in a decrease in the corrosion current density (i_{corr}), while the potential remains relatively stable at approximately −0.248 V and −0.2003 V. This indicates that the inhibitor remains effective and enhances film adsorption on the surface of P9.

The Nyquist plot indicates a single semicircle capacitive loop for the uninhibited system, signifying charge transfer. For solutions with 20–80 ppm EE, the loop diameter increases compared to the blank, confirming an increase in P9 steel impedance. This correlates with the active functional groups of EE, such as aromatic alcohols, C=C, C=O, and -OH, which adsorb onto the alloy surface, reducing metal dissolution and hindering electrochemical reactions (Fig. 4). Additionally, a long linear tail at 2000–1600 Ω in the low-frequency region suggests a diffusion-controlled process, indicating mass transport buildup [42].

The approximately 45° angle demonstrates that higher inhibitor concentration slows corrosion, reflecting the presence of a mixed-type inhibitor. Furthermore, the distortion of the capacitive arc at 20, 40, and 80 ppm correlates with the surface roughness of corrosion products and heterogeneity at the interface between the electrode and the electrolyte. In this context, the electrical circuit depicted in Fig. 7 displays the presence of R_s (solution resistance), R_{inh} (inhibitor resistance), and *CPE* (Constant Phase Element), representing the non-ideal electrochemical characteristics where the double-layer capacitance is replaced by the *CPE*. The components of the *CPE*, n and Y_0, are attributable to surface roughness and system passivity. The increase in R_{inh} and the decrease of n to 0.702 demonstrate higher inhibition efficiency, quantified at 77.38% at 333K with 80 ppm of EE inhibitor, while simultaneously enhancing the surface heterogeneity of the P9 steel and causing the system to behave as a non-ideal capacitor, thereby storing less electrical charge. It is also evident that there exists a negative proportionality between R_{inh} and Y_0 across all concentrations, indicative of a reduction in the local dielectric constant and an increase in the thickness of the passive double-layer film due to EE inhibitor adsorption. This process displaces water molecules, which are replaced by inhibitor molecules, resulting in a thicker protective passive film as the inhibitor concentration increases [43].

Additionally, the Bode plot demonstrates a positive correlation between the absolute impedance and inhibitor concentration, signifying enhanced protection afforded by the EE inhibitor. The Bode plot confirms this, showing increased impedance in the range of 1.4 to 3.8 $\Omega \cdot cm^2$ in the inhibited system compared to the blank, with a decreasing trend from 3.3 to 1.5 $\Omega \cdot cm^2$. This interaction implies active functional groups occupy the P9 surface, particularly in the anodic and cathodic regions, before intensive passivation occurs. The Bode modulus results, approaching 70°, suggest strong capacitive behavior due to the formation of a dense, uniform protective inhibitor film [44].

This observation also correlates with the increase in R_{inh}, inhibition efficiency, and the depression of R_s. The impedance modulus and phase angle values exhibit an upward trend with increasing concentration and temperature. This phenomenon is consistent with the variation of the capacitance loop diameter as the temperature rises. The Bode phase angle in the inhibited system broadens as concentration increases, indicating surface heterogeneity and an acceleration of charge transfer during diffusion. Additionally, this supports the results of Y_0 and n as illustrated in Table 3. However, it is critical to examine the inhibitor's thermal stability and its stability at elevated temperatures, as demonstrated by thermodynamic calculations (Table 4).

Thermodynamic analysis indicates that the inhibitors act primarily as chemisorption inhibitors, evidenced by the low ΔG_{ads} and ΔS_{ads} values and increased surface coverage. It is also worth noting that the negative ΔG_{ads} value indicates the adsorption process occurs spontaneously. Moreover, the values of ΔG_{ads} and ΔH_{ads} are consistent with a chemisorption mechanism, where the interaction between surface P9 and the inhibitor is more potent. The immense ΔH_{ads} value of +26.7252 kJ/mol shows that energy is absorbed during inhibitor adsorption, which is required to break the surface bonds between the P9 metal and water, as well as between the P9 metal and the oxide layer in the uninhibited system before adsorbate dissociation and electron transfer [45]. The higher ΔH_{ads} value further confirms that adsorption is more favorable at elevated temperatures and supports the modeling of the inhibition mechanism under naphthenic acid corrosion. Additionally, the adsorption equilibrium constant K_{ads} reaches a maximum of 0.0427, confirming strong adsorption of the eco-enzyme at the surface, thereby reducing bonding between iron ions and the naphthenic acid residue. In addition, a single thicker protective layer forms, reducing pitting corrosion on P9 steel.

Fig. 8, *a* characterizes the feature of naphthenic acid corrosion, where the presence of localized corrosion and pitting corrosion is uniform and severe, particularly in the darker areas. In this context, pitting corrosion results in a rougher surface and more profound attack from the oil phase, becoming notably localized and isolated in the form of character-shaped pits (Fig. 8, *a*). Furthermore, the anodic dissolution caused by the reaction between P9 alloy and naphthenic acid extract indicates localized attack at the anodic region of the water phase; however, this effect gradually diminishes in the oil phase. It is hypothesized that the increased weak acid concentration at the oil-water interface facilitates diffusion within the crude oil phase. Concurrently, the elevated oxygen content, as evidenced by the EDX analysis indicating approximately 50.08% wt., correlates with the high solubility of oxygen in oil and subsequently promotes galvanic processes between the crude oil and aqueous phases (Fig. 9, *a*) [46]. Accordingly, the most plausible explanation for the localized corrosion is the higher concentration of naphthenic acid extract in the upper aqueous layer, which is proximate to the oil phase.

Conversely, the hydrophobic character of the inhibitor, attributable to the presence of aromatic compounds, induces water repulsion and ion exclusion, resulting in a smoother surface with reduced oil dissipation and enhanced film stability capable of covering surface pits on P9 steel (Fig. 8, *b*).

Additionally, the results demonstrate a more continuous and compact coating, which reduces oil diffusion onto the P9 surface, thereby suggesting that the formation of a protective inhibitor layer decreases the sulfur content from 3.09 wt.% to 1.08 wt.% in the inhibited system. Simultaneously, increasing the iron content to 69.41 wt.% and the oxygen content to 11.58 wt.% within the same system indicates a reduced risk of naphthenic acid corrosion. The inhibitor effectively minimizes FeS scale formation, as evidenced by SEM-EDX results showing that sulfur content decreases with inhibitor addition (Fig. 9, *b*) [47].

It is also essential to recognize the practical significance of the findings concerning the scale-up of the eco-enzyme inhibitor to the HVGO pipeline within the crude distillation unit. The high inhibition efficiency observed, nearly 78%, along with the extensive surface coverage, indicates that the inhibitor effectively safeguards the P9 material from the risk of naphthenic acid corrosion. This scope pertains to the simulation of a non-commercial inhibitor, despite the limited injection schedule available. The injection parameters should be determined based on corrosion monitoring results from the identified line, where the corrosion rate is moderate to high. Consequently, in practical applications, injection can be scheduled using various inhibitor concentrations to reduce corrosion rate. Nonetheless, corrosion monitoring along the piping line should also be maintained to ensure the proper dosage and film persistence within the inhibitor simulation injection.

Despite the notable outcomes, this study possesses certain limitations. It encompasses the contribution of phenolic hydroxyl and other functional groups identified through the functional group test as components of the EE inhibitor, although additional active compounds may be present. Furthermore, the investigation does not elucidate the precise mechanism by which molasses influences enzyme production as a preservative or its function as a pH regulator. Additionally, the crude oil employed contains an overall sulfur content of 0.19%. It is also important to acknowledge that measurements were confined to a temperature of 60°C, which may only marginally simulate the NAC within a laboratory environment. This disadvantage lead to opportunity to conduct the mass-spectrophotometer and hydrogen-nuclear magnetic resonance test to unveil the actual molecular mass and actual structure of the EE inhibitor corresponding to the inhibition mechanism. It leads to the develop the experimental method to characterize the actual functional group that dwells in the inhibitor which resemble the corrosion inhibition process.

7. Conclusion

1. The presence of Chromium and Molybdenum are identified in the P9 material in fact their chemical composition decreases when simulated in NA distillate to compensate the anti-corrosion performance.

2. The ultimate critical factor of the passive film based on the adsorption of phenol -OH, C=C, C=O, RCHO, conjugated C=O, C-O, and benzene to enhance the adsorption of inhibitor. Moreover, the electronic transition n-π^* and π-π^* at 350 nm correlates to amphiphilic (hydrophilicity and hydrophobicity of the inhibitor) benzene and carbonyl, while the absorption at 300–400 nm corresponds to the metal-to-ligand charge transfer.

3. The inhibitor shows remarkable inhibition efficiency beyond 77% that attributed with the increase of inhibitor resistance, depression of charge transfer resistance, despite their surface heterogeneity increases measured of 80 ppm inhibitor solution at 333K.

4. The thermodynamic results indicate that the changes in enthalpy, entropy, and Gibbs free energy are +26.7252 kJ/mol, +168.91 kJ/mol, and –29.5236 kJ/mol, respectively. These values are consistent with chemisorption adsorption. Furthermore, the R^2 value approaching 1 exemplifies the formation of a monolayer inhibitor film and conforms to the Langmuir isotherm adsorption model.

5. The formation of a single passive layer enhances the surface smoothness of P9 steel by reducing the percentages of S and O, while increasing the Fe content, as shown in SEM-EDX results. This is used to model how the EE inhibitor mitigates the risk of NA at elevated temperatures, which reduces the pitting corrosion.

Conflict of interest

The authors declare that they have no conflict of interest in relation to this study, whether financial, personal, authorship, or otherwise, that could affect the study and its results presented in this paper.

Financing

The study was performed without financial support.

Data availability

Data cannot be made available for reasons disclosed in the data availability statement.

Use of artificial intelligence

The authors confirm that they did not use artificial intelligence technologies in creating the submitted work.

Authors' contributions

Kadek Jaya: Writing original manuscript, Data curation, Formal analysis, Methodology; **Johny Soedarsono**: Formal analysis, investigation, resources, supervision; **Yudha Pratesa**: Validation, Review and Editing, Supervision, Investigation; **Rini Riastuti**: Investigation, Methodology, Resources, Supervision; **Agus Kaban**: Formal Analysis, Investigation, Review and Editing, Supervision.

References

1. Rodríguez-Antón, L. M., Gutiérrez-Martín, F., Martinez-Arevalo, C. (2015). Experimental determination of some physical properties of gasoline, ethanol and ETBE ternary blends. Fuel, 156, 81–86. https://doi.org/10.1016/j.fuel.2015.04.040

2. Esouilem, M., Bouzid, A.-H., Nadeau, S. (2022). Pressure Vessels and Piping Accident Analysis and Prevention: A Case Study in Canada. International Journal of Safety and Security Engineering, 12 (1), 105–114. https://doi.org/10.18280/ijsse.120113
3. Stepanova, N. E. (2022). Environmental safety and environmental protection at an oil refinery. Advances in Current Natural Sciences, 5, 78–83. https://doi.org/10.17513/use.37828
4. Rajaram, K., Jaikumar, R., Behlau, F., van Esch, F., Heynen, C., Kaiser, R. et al. (1999). Robust Process Control at Cerestar's Refineries. Interfaces, 29 (1), 30–48. https://doi.org/10.1287/inte.29.1.30
5. Sukcharoen, K., Leatham, D. J. (2017). Hedging downside risk of oil refineries: A vine copula approach. Energy Economics, 66, 493–507. https://doi.org/10.1016/j.eneco.2017.07.012
6. Verma, C., Ebenso, E. E., Quraishi, M. A. (2017). Corrosion inhibitors for ferrous and non-ferrous metals and alloys in ionic sodium chloride solutions: A review. Journal of Molecular Liquids, 248, 927–942. https://doi.org/10.1016/j.molliq.2017.10.094
7. Siler-Evans, K., Hanson, A., Sunday, C., Leonard, N., Tumminello, M. (2014). Analysis of pipeline accidents in the United States from 1968 to 2009. International Journal of Critical Infrastructure Protection, 7 (4), 257–269. https://doi.org/10.1016/j.ijcip.2014.09.002
8. Matthews, C. (2023). API RP 571: Damage Mechanisms (API 653). The API ICP Exam Handbook: Complete Guide to Passing the API 510/570/653 ICP Exams, 792–800. https://doi.org/10.1115/1.862api_ch38
9. Qu, D., Zheng, Y., Jiang, X., Ke, W. (2007). Correlation between the corrosivity of naphthenic acids and their chemical structures. Anti-Corrosion Methods and Materials, 54 (4), 211–218. https://doi.org/10.1108/00035590710762348
10. Chakravarthy, R., Naik, G. N., Savalia, A., Sridharan, U., Saravanan, C., Das, A. K., Gudasi, K. B. (2016). Determination of Naphthenic Acid Number in Petroleum Crude Oils and Their Fractions by Mid-Fourier Transform Infrared Spectroscopy. Energy & Fuels, 30 (10), 8579–8586. https://doi.org/10.1021/acs.energyfuels.6b01766
11. Qu, D. R., Zheng, Y. G., Jing, H. M., Yao, Z. M., Ke, W. (2006). High temperature naphthenic acid corrosion and sulphidic corrosion of Q235 and 5Cr1/2Mo steels in synthetic refining media. Corrosion Science, 48 (8), 1960–1985. https://doi.org/10.1016/j.corsci.2005.08.016
12. Moura, L. B., Guimarães, R. F., Abreu, H. F. G. de, Miranda, H. C. de, Tavares, S. S. M. (2012). Naphthenic corrosion resistance, mechanical properties and microstructure evolution of experimental Cr-Mo steels with high Mo content. Materials Research, 15 (2), 277–284. https://doi.org/10.1590/s1516-14392012005000024
13. Huang, B. S., Li, H., Liu, Q. Y., Ma, X., Wang, Y. (2009). Inhibitor of naphthenic acid corrosion in atmospheric and vacuum distillation unit. Corrosion & Protection, 30 (10), 721–723. Available at: https://www.mat-test.com/en/article/id/5fa03a84-16a8-4975-9869-9e40a292caff
14. Sun, M., Nicosia, D., Prins, R. (2003). The effects of fluorine, phosphate and chelating agents on hydrotreating catalysts and catalysis. Catalysis Today, 86 (1-4), 173–189. https://doi.org/10.1016/s0920-5861(03)00410-3
15. Salem, S. M., Abdelaleem, G. M., Elsayed, N. A., Saad, W. O. (2011). Improving the qality of petroleum crude oils by deasphalting. JES. Journal of Engineering Sciences, 39 (4), 885–896. https://doi.org/10.21608/jesaun.2011.127722
16. Tang, C., Farhadian, A., Berisha, A., Deyab, M. A., Chen, J., Iravani, D. et al. (2022). Novel Biosurfactants for Effective Inhibition of Gas Hydrate Agglomeration and Corrosion in Offshore Oil and Gas Pipelines. ACS Sustainable Chemistry & Engineering, 11 (1), 353–367. https://doi.org/10.1021/acssuschemeng.2c05716
17. Wang, Q., Wang, R., Zhang, Q., Zhao, C., Zhou, X., Zheng, H. et al. (2023). Application of Biomass Corrosion Inhibitors in Metal Corrosion Control: A Review. Molecules, 28 (6), 2832. https://doi.org/10.3390/molecules28062832
18. Kaban, A. P. S., Ridhova, A., Priyotomo, G., Elya, B., Maksum, A., Sadeli, Y. et al. (2021). Development of white tea extract as green corrosion inhibitor in mild steel under 1 M hydrochloric acid solution. Eastern-European Journal of Enterprise Technologies, 2 (6 (110)), 6–20. https://doi.org/10.15587/1729-4061.2021.224435
19. Riastuti, R., Mashanafie, G., Rizkia, V., Maksum, A., Prifiharni, S., Kaban, A. et al. (2022). Effect of syzygium cumini leaf extract as a green corrosion inhibitor on API 5l carbon steel in 1M HCL. Eastern-European Journal of Enterprise Technologies, 6 (6 (120)), 30–41. https://doi.org/10.15587/1729-4061.2022.267232
20. Muliarta, I. N., Darmawan, I. K. (2021). Processing Household Organic Waste into Eco-Enzyme as an Effort to Realize Zero Waste. Agriwar Journal, 1 (1), 6–11.
21. Moradi, M., Topchiy, E., Lehmann, T. E., Alvarado, V. (2013). Impact of ionic strength on partitioning of naphthenic acids in water–crude oil systems – Determination through high-field NMR spectroscopy. Fuel, 112, 236–248. https://doi.org/10.1016/j.fuel.2013.05.024
22. ASTM G5-94(1999)e1. Standard Reference Test Method for Making Potentiostatic and Potentiodynamic Anodic Polarization Measurements. https://doi.org/10.1520/g0005-94r99e01
23. Soedarsono, J. W., Shihab, M. N., Azmi, M. F., Maksum, A. (2018). Study of curcuma xanthorrhiza extract as green inhibitor for API 5L X42 steel in 1M HCl solution. IOP Conference Series: Earth and Environmental Science, 105, 012060. https://doi.org/10.1088/1755-1315/105/1/012060
24. Jayakumar, S., Nandakumar, T., Vadivel, M., Thinaharan, C., George, R. P., Philip, J. (2019). Corrosion inhibition of mild steel in 1M HCl usingTamarindus indicaextract: electrochemical, surface and spectroscopic studies. Journal of Adhesion Science and Technology, 34 (7), 713–743. https://doi.org/10.1080/01694243.2019.1681156
25. Vorobyova, V., Skiba, M. (2024). Mechanism of inhibitory action of fruit cake extracts as a new environmentally inhibitors of carbon steel corrosion. Results in Chemistry, 7, 101317. https://doi.org/10.1016/j.rechem.2024.101317

26. Li, Y., Xu, W., Lai, J., Qiang, S. (2022). Inhibition Effect and Mechanism Explanation of Perilla Seed Extract as a Green Corrosion Inhibitor on Q235 Carbon Steel. Materials, 15 (15), 5394. https://doi.org/10.3390/ma15155394
27. Liao, B., Ma, S., Zhang, S., Li, X., Quan, R., Wan, S., Guo, X. (2023). Fructus cannabis protein extract powder as a green and high effective corrosion inhibitor for Q235 carbon steel in 1 M HCl solution. International Journal of Biological Macromolecules, 239, 124358. https://doi.org/10.1016/j.ijbiomac.2023.124358
28. Arslanhan, S., Sığırcık, G., Yıldız, R., Baran, M. F. (2024). Lavandula angustifolia Extract as a Green Corrosion Inhibitor for Protection of Mild Steel in HCl Acid Solution. Protection of Metals and Physical Chemistry of Surfaces, 60 (3), 554–570. https://doi.org/10.1134/s2070205124701739
29. Banda-Cruz, E. E., Gallardo-Rivas, N. V., Martínez-Orozco, R. D., Páramo-García, U., Mendoza-Martínez, A. M. (2021). Derivative UV-Vis Spectroscopy of Crude Oil and Asphaltene Solutions for Composition Determination. Journal of Applied Spectroscopy, 87 (6), 1157–1162. https://doi.org/10.1007/s10812-021-01124-4
30. Lin, T.-C., Cole, J. M., Higginbotham, A. P., Edwards, A. J., Piltz, R. O., Pérez-Moreno, J. et al. (2013). Molecular Origins of the High-Performance Nonlinear Optical Susceptibility in a Phenolic Polyene Chromophore: Electron Density Distributions, Hydrogen Bonding, and ab Initio Calculations. The Journal of Physical Chemistry C, 117 (18), 9416–9430. https://doi.org/10.1021/jp400648q
31. Kochowski, S., Nitsch, K. (2002). Description of the frequency behaviour of metal–SiO2–GaAs structure characteristics by electrical equivalent circuit with constant phase element. Thin Solid Films, 415 (1-2), 133–137. https://doi.org/10.1016/s0040-6090(02)00506-0
32. Elaraby, A., El-samad, Shrouk. A., khamis, Eman. A., Zaki, E. G. (2023). Theoretical and electrochemical evaluation of tetra-cationic surfactant as corrosion inhibitor for carbon steel in 1 M HCl. Scientific Reports, 13 (1). https://doi.org/10.1038/s41598-023-27513-7
33. Vashishth, P., Bairagi, H., Narang, R., Shukla, S. K., Mangla, B. (2022). Thermodynamic and electrochemical investigation of inhibition efficiency of green corrosion inhibitor and its comparison with synthetic dyes on MS in acidic medium. Journal of Molecular Liquids, 365, 120042. https://doi.org/10.1016/j.molliq.2022.120042
34. Sedik, A., Lerari, D., Salci, A., Athmani, S., Bachari, K., Gecibesler, İ. H., Solmaz, R. (2020). Dardagan Fruit extract as eco-friendly corrosion inhibitor for mild steel in 1 M HCl: Electrochemical and surface morphological studies. Journal of the Taiwan Institute of Chemical Engineers, 107, 189–200. https://doi.org/10.1016/j.jtice.2019.12.006
35. Li, X.-H., Deng, S.-D., Fu, H. (2010). Inhibition by Jasminum nudiflorum Lindl. leaves extract of the corrosion of cold rolled steel in hydrochloric acid solution. Journal of Applied Electrochemistry, 40 (9), 1641–1649. https://doi.org/10.1007/s10800-010-0151-5
36. Kaban, A. P. S., Soedarsono, J. W., Mayangsari, W., Anwar, M. S., Maksum, A., Ridhova, A., Riastuti, R. (2023). Insight on Corrosion Prevention of C1018 in 1.0 M Hydrochloric Acid Using Liquid Smoke of Rice Husk Ash: Electrochemical, Surface Analysis, and Deep Learning Studies. Coatings, 13 (1), 136. https://doi.org/10.3390/coatings13010136
37. Xhanari, K., Finšgar, M., Knez Hrnčič, M., Maver, U., Knez, Ž., Seiti, B. (2017). Green corrosion inhibitors for aluminium and its alloys: a review. RSC Advances, 7 (44), 27299–27330. https://doi.org/10.1039/c7ra03944a
38. Al Otaibi, N., Hammud, H. H. (2021). Corrosion Inhibition Using Harmal Leaf Extract as an Eco-Friendly Corrosion Inhibitor. Molecules, 26 (22), 7024. https://doi.org/10.3390/molecules26227024
39. Huang, J., Hu, J., Cai, J., Huang, H., Wei, J., Yu, Q. (2022). Inhibition Effect of Hydrophobic Functional Organic Corrosion Inhibitor in Reinforced Concrete. Materials, 15 (20), 7124. https://doi.org/10.3390/ma15207124
40. Raja, P. B., Qureshi, A. K., Abdul Rahim, A., Osman, H., Awang, K. (2013). Neolamarckia cadamba alkaloids as eco-friendly corrosion inhibitors for mild steel in 1M HCl media. Corrosion Science, 69, 292–301. https://doi.org/10.1016/j.corsci.2012.11.042
41. Zou, Z., Liu, Z., Yang, L., Tang, Y., Qiao, Y., Lu, D. (2024). Corrosion behavior of different building planes of selective laser melting 316L stainless steel in 0.1 M HCl solution. Journal of Materials Research and Technology, 28, 4738–4753. https://doi.org/10.1016/j.jmrt.2024.01.078
42. Yadav, A. K., Pandey, R., Singh, P. (2025). Impedance spectroscopy in perovskite materials: From fundamentals to applications. Inorganic Chemistry Communications, 182, 115524. https://doi.org/10.1016/j.inoche.2025.115524
43. Meng, Y., Li, S., Zhang, Z. (2024). Inhibition performance of uniconazole on steel corrosion in simulated concrete pore solution: An eco-friendly way for steel protection. Heliyon, 10 (3), e24688. https://doi.org/10.1016/j.heliyon.2024.e24688
44. Tang, Z., Huang, W., Liu, L., Li, H., Meng, H., Zeng, T. et al. (2024). Study on structure and molecular scale protection mechanism of green Ce,N-CDs anti-bacterial and anti-corrosive inhibitor. Journal of Materials Research and Technology, 28, 3865–3881. https://doi.org/10.1016/j.jmrt.2023.12.250
45. Mabrouk, D. H., El-Morsy, F. E., Alsam, A. A. (2024). Electrochemical studies, adsorption behavior, and spectroscopic analysis of vanadyl complex of bis(1-(pyridin-2-yl)ethylidene)malonohydrazide as efficient eco-friendly corrosion inhibitor for low carbon steel in 1M HCl. International Journal of Electrochemical Science, 19 (5), 100528. https://doi.org/10.1016/j.ijoes.2024.100528
46. Silva, R. M. P., Suffredini, H. B., Bastos, I. N., Santos, L. F., Simões, A. M. P. (2022). Naphthenic acid corrosion of API 5L X70 steel in aqueous/oil environment using electrochemical surface-resolved and analytical techniques. Electrochimica Acta, 407, 139900. https://doi.org/10.1016/j.electacta.2022.139900
47. Pessu, F., Barker, R., Chang, F., Chen, T., Neville, A. (2021). Iron sulphide formation and interaction with corrosion inhibitor in H_2S-containing environments. Journal of Petroleum Science and Engineering, 207, 109152. https://doi.org/10.1016/j.petrol.2021.109152